SANDIA REPORT

SAND2014-20268
Unlimited Release
Printed March 2015

Multiphysics Model of Palladium Hydride Isotope Exchange Accounting for Higher Dimensionality

Patricia E. Gharagozloo, Mehdi Eliassi, and Brad Bon

Prepared by
Sandia National Laboratories
Albuquerque, New Mexico 87185 and Livermore, California 94550

Sandia National Laboratories is a multi-program laboratory managed and operated by Sandia Corporation, a wholly owned subsidiary of Lockheed Martin Corporation, for the U.S. Department of Energy's National Nuclear Security Administration under contract DE-AC04-94AL85000.

Issued by Sandia National Laboratories, operated for the United States Department of Energy by Sandia Corporation.

Available to DOE and DOE contractors from
U.S. Department of Energy
Office of Scientific and Technical Information
P.O. Box 62
Oak Ridge, TN 37831

Telephone: (865) 576-8401
Facsimile: (865) 576-5728
E-Mail: reports@adonis.osti.gov
Online ordering: http://www.osti.gov/bridge

Available to the public from
U.S. Department of Commerce
National Technical Information Service
5285 Port Royal Rd.
Springfield, VA 22161

Telephone: (800) 553-6847
Facsimile: (703) 605-6900
E-Mail: orders@ntis.fedworld.gov
Online order: http://www.ntis.gov/help/ordermethods.asp?loc=7-4-0#online

SAND2014-20268
Unlimited Release
Printed March 2015

Multiphysics Model of Palladium Hydride Isotope Exchange Accounting for Higher Dimensionality

Patricia E. Gharagozloo
Thermal/Fluid Science & Engineering, 08365

Mehdi Eliassi
Phenomenology and Sensors Department, 05713

Brad Bon

Sandia National Laboratories
P.O. Box 5800
Albuquerque, New Mexico 87185-MS0406

ABSTRACT

This report summarizes computational model development and simulations results for a series of isotope exchange dynamics experiments including long and thin isothermal beds similar to the Foltz and Melius beds and a larger non-isothermal experiment on the NENG7 test bed. The multiphysics 2D axi-symmetric model simulates the temperature and pressure dependent exchange reaction kinetics, pressure and isotope dependent stoichiometry, heat generation from the reaction, reacting gas flow through porous media, and non-uniformities in the bed permeability. The new model is now able to replicate the curved reaction front and asymmetry of the exit gas mass fractions over time. The improved understanding of the exchange process and its dependence on the non-uniform bed properties and temperatures in these larger systems is critical to the future design of such systems.

ACKNOWLEDGMENTS

This work was funded by Sandia National Laboratories through Physics and Engineering Models (P&EM) as a part of ASC program. This work greatly benefited from the discussions with Steve Rice and Bradley Bon (08254), David Robinson (08651), and Maher Salloum (8961). We would also like to thank Steve Rice for providing the experimental data for various NENG-7 experiments, which we used to test our computational models. Finally, we appreciate all the foundational work done by Scott James (former Sandia staff) on developing the preliminary COMSOL models.

We would also like to thank Paul Spence, Greg Wagner, Chris Moen for advice and program guidance.

CONTENTS

Contents

FIGURES

TABLES

NOMENCLATURE

A_s	specific surface area
c_f	sticking probability calibration factor
c_p	specific heat capacity
d	mean particle diameter
D	deuterium
D_i	diffusion coefficient of i
F_r	Radial bed permeability variation
F_z	Axial bed permeability variation
H	hydrogen
H_i	enthalpy of i
ΔH_i	heat of reaction of i
J_i	flux of i
K_i	thermal conductivity of i
k_i	equilibrium constant for reaction i
L	bed axial length
M_i	molar mass of i
N_s	surface species concentration
p	pressure
p_f	permeability calibration factor
Pd	palladium
Q	heat source
Q_m	mass source
R	bed radius
R_g	universal gas constant
R_i	production rate of i
t	time
T	temperature
u	velocity
V_b	bulk vacancy
V_s	surface vacancy
v_t	thermal velocity
x_i	mole fraction of i

Greek alphabet

α	isotope exchange coefficient
θ	bed porosity
κ	bed permeability
κ_{cl}	bed permeability at center line
μ	gas dynamic viscosity
ρ	density
ω_i	mass fraction of i

1. Introduction

It has long been known that hydrogen and its isotopes (e.g., H and D) readily dissolve in certain metals, notably palladium (Pd) [1, 2, and 3]. Due to small differences in thermochemistry, one isotope is generally stored preferentially over the other [4], thereby making separations possible. Alternatively, storage itself may be the primary goal, with one isotope being used to flush out the other when needed. Measured and controlled hydrogen isotope exchange with Pd is in fact routinely carried out, but the physical and chemical aspects of this process are not yet fully understood.

Palladium hydride can exist in two distinct phases, α and β. However, the former is capable of storing only small amounts of hydrogen (up to perhaps $PdH_{0.02}$ around room temperature) and is of no interest here. At room temperature and pressures near atmospheric, only the β phase can exist, with a stoichiometry of roughly $PdH_{0.7}$. The equilibrium hydrogen content decreases modestly with temperature and increases slowly with pressure. It is, of course, this phase that is used in storage applications. Quantitative equilibrium data in the form of pressure-concentration-temperature plots are available [5 and 6].

The dissolution of hydrogen isotopes in both the α [7, 8, and 9] and β [10, 11, and 12] phases has been studied to determine diffusion rates for H and D in the solid. However, for most systems of interest, exchange rates are limited not by diffusion but by surface reactions; only for large Pd particles at low temperatures does the former limit the exchange [13, 14, and 15]. Many researchers have examined specific aspects of the exchange process [16, 17, 18, 19, 20, 21, and 22], and still others have proposed mathematical models [23, 24, 25, 26, and 27], but significant uncertainties remain with regard to the physics and chemistry that must be included to yield a predictive model. For example, is surface kinetics or bulk diffusion the rate limiting mechanism? Are there important differences between surface and bulk site in the Pd? Do surface and gas-phase species exchange directly, or is it a multi-step process? Can the complex physics be accurately simulated with simpler models?

In this research effort, a model was developed to simulate H and D exchanged over a powdered β-Pd bed. Both D→H (exothermic replacement of dissolved D with H) and H→D (endothermic replacement of dissolved H with D) are simulated here with the same reaction mechanism (all steps being reversible). For example, Foltz and Melius (F&M) [28 and 29] conducted both D→H and H→D exchange experiments and these data were used to verify and calibrate the exchange model. In this work, hydrogen and deuterium isotopes exchange was simulated using the commercial finite element code, COMSOL [30]. Because the F&M experiments were nearly isothermal and isobaric, they serve as excellent data sets with which to develop a simplified model that is later extended to more complex exchange systems with significant pressure and temperature excursions.

The isothermal model matches well at room and high temperatures. However, for the cold temperature case, the model does not match well. This is likely due to the limiting exchange mechanism transitioning from surface kinetics to bulk diffusion for these colder temperatures. With the verified reaction kinetics for room and high temperature regimes with the isothermal

experiments, the model is expanded to the more complex multi-scale, non-isothermal experimental set-up called NENG-7.

2. Governing Equations

Since our modeling and simulations of isotope exchange involves flow, chemical transport, chemical kinetics, and heat transfer, we must solve a set of highly coupled equations. As noted previously, our model uses the COMSOL [30] multi-physics framework to numerically solve the equations being discussed in this section. Moreover, while all our simulations are in two-dimensional axi-symmetric geometry, for completeness, we state the general form of the equations in the following sections.

2.1. Flow

We use the standard Darcy flux equation to model the flow of compressible, non-isothermal gas flow through a packed Pd bed. In general, the conservation of mass equation can be written as:

$$\frac{\partial}{\partial \mathrm{t}}(\theta\rho) + \nabla \cdot (\rho\vec{u}) = Q_m \tag{1}$$

where t (sec) is time, θ is the Pd bed porosity, ρ (g/cm^3) is the mixture gas density, $\vec{u}$ (cm/sec) is the velocity vector, and Q_m (g/cm^3-s) is the volumetric mass source. In absence of gravity, Darcy flux equation can be stated as:

$$\vec{u} = -\frac{k}{\mu}\nabla p \tag{2}$$

where k (cm^2) is the bed permeability, μ (g/cm-s) is the mixture gas dynamic viscosity, and p (barye or dynes/cm^2).

Bed Permeability

The basic form of the permeability, in this work, is based on *Carman-Kozeny* equation, as stated in Kaviany [31]:

$$\kappa = \frac{\theta^3}{180(1-\theta)^2} d^2 \tag{3}$$

Where κ (cm^2) is the permeability, d=6/A_s (cm) is the mean particle diameter, and A_s (1/cm) is the particle specific surface. For packed bed of spherical particles having a narrow size distribution, Kaviany [31] suggests:

$$\kappa = \frac{\theta^{5.5}}{5.6} d^2 \tag{4}$$

While Eq. 3 and Eq. 4 treat the bed permeability as constant, the packing process causes the permeability to vary axially and radially. To estimate this non-uniformity a simple spatially varying form of the permeability model:

$$\boldsymbol{\kappa}\left(\frac{r}{R},\frac{z}{L}\right)=\frac{\kappa_{cl}}{F_1\left(\frac{z}{L}\right)F_2\left(\frac{r}{R}\right)} \tag{5}$$

where κ_{cl} (cm^2) is the permeability along the bed center-line (e.g., Eq. 3 and Eq. 4), R (cm) and L (cm) refer to the bed radius and length, respectively, and F_1 and F_2 have the forms:

$$F_1\left(\frac{z}{L}\right)=1-(1-b_1)\left(\frac{z}{L}\right) \quad \text{and } F_2\left(\frac{r}{L}\right)=b_2+(1-b_2)\left[1-\left(\frac{r}{R}\right)^2\right] \tag{6}$$

where b_1 and b_2, are dimensionless constants. Note that when b_1=b_2=1, Eq. 6 reduces to a constant. When using this formula, it is important to adjust κ_{cl} to ensure the average permeability stays the same between cases.

Mixture Gas Viscosity

The viscosity for the three gases (i.e., H_2, HD, D_2) is found using Wilke's formula [32]:

$$\boldsymbol{\mu}=\sum_{i=1}^{3}\frac{\mu_i}{1+\frac{1}{\rho_i}\sum_{j=1,j\neq i}^{3}\rho_j\xi_{ij}} \tag{7}$$

where indices i and j refer to each gas and

$$\xi_{ij}=\frac{\left[1+\left(\frac{\mu_i}{\mu_j}\right)^{1/2}\left(\frac{M_j}{M_i}\right)^{1/2}\right]^2}{\frac{4}{\sqrt{2}}\left(1+\frac{M_i}{M_j}\right)^{1/2}} \tag{8}$$

where M_i (g/mole) refers to the molar mass of each gas. We should note that to evaluate the hydrogen viscosity, we use the Sutherland's relationship:

$$\boldsymbol{\mu_{H_2}}=\boldsymbol{\mu_0}\left(\frac{T}{T_0}\right)^{n} \tag{9}$$

Where μ_0=8.411x10^{-5} (g/cm-s), T_0=273.15 (K), T (K) is the temperature, and n=0.68. The viscosities for the other two gases are scaled using hydrogen viscosity as: $\mu_{D_2}=\mu_{H_2}\sqrt{M_{D_2}/M_{H_2}}$ with HD viscosity being evaluated similarly.

Mixture Gas Density

We evaluate the gas (mixture) density, based on the ideal gas law, based on the mass fraction the various gases, or:

$$\boldsymbol{\rho}=\boldsymbol{\rho_g}=\frac{P}{R_gT}\left([\boldsymbol{H_2}]\boldsymbol{M_{H_2}}+[\boldsymbol{HD}]\boldsymbol{M_{HD}}+[\boldsymbol{D_2}]\boldsymbol{M_{D_2}}\right) \tag{10}$$

Where R_g=8.314 (J/mol-K) is the universal gas constant, and [H_2], [HD], and [D_2] refer to the mole fraction of each isotope.

Volumetric Mass Source

In this work, we represent the volumetric mass source, as the sum of the production/depletion rate of each isotope times the corresponding atomic mass of the isotope or:

$$\mathbf{Q_m = S_A\left[\dot{H}_2 M_{H_2} + \dot{D}_2 M_{D_2} + \dot{HD} M_{HD}\right]} \tag{11}$$

where M_i (g/mole) refers to the molar mass of each isotope and the various rate equation (mol/cm^2-sec) are as follows:

$$\mathbf{\dot{H}_2 = k_2\left[\widetilde{HD}\right][H_s] - k_{-2}\left[\widetilde{H_2}\right][D_s]}, \tag{12}$$

$$\mathbf{\dot{D}_2 = -k_1\left[\widetilde{D_2}\right][H_s] + k_{-1}\left[\widetilde{HD}\right][D_s]}, \text{ and} \tag{13}$$

$$\mathbf{\dot{HD} = -k_2\left[\widetilde{HD}\right][H_s] + k_{-2}\left[\widetilde{H_2}\right][D_s] + k_1\left[\widetilde{D_2}\right][H_s] - k_{-1}\left[\widetilde{HD}\right][D_s]}. \tag{14}$$

where coefficient k's (cm^3/mol-s) are the kinetic reaction rates, $\left[\widetilde{HD}\right]$, $\left[\widetilde{H_2}\right]$, and $\left[\widetilde{D_2}\right]$ (mol/cm^3) are the molar densities of HD, H_2, and D_2, respectively. Moreover, $[H_s]$ and $[D_s]$ (mol/cm^2) are referred to as the adsorbed isotope concentrations. The relationships for k's as well as the equations for $[H_s]$ and $[D_s]$ are described in the Section 2.3.

2.2. Species Transport

To study the process of isotope exchange in a porous palladium bed, we used "The Transport of Concentrated Species Interface" in COMSOL 4.3 [30]. This interface can be used to model the evolution of concentrated solutions or gas mixtures due to advection and diffusion. The conservation of species equation can be written as:

$$\mathbf{\frac{\partial}{\partial t}(\rho\omega_i) + \nabla\cdot(\rho\omega_i\vec{u}) = -\nabla\cdot\vec{J_i} + R_i} \tag{15}$$

where ρ is the gas mixture density, ω_i (-) is the mass fraction for each species, i=H_2, D_2, and HD, $\mathbf{\vec{J}_i}$ (gm/cm-s) is the generalized transport flux vector and R_i (gm/cm^2-s) is the production rate of i. COMSOL 4.2a provides several options for $\boldsymbol{J_i}$ which include Maxwell-Stefan (MS), Mixture-averaged, and Fick's law. For this work, while we attempted to first use the MS equation, we found the simulated isotope mass fractions and molar concentrations using MS were incorrect. However, the Fick's law model appeared to produce correct results. The mass flux vector for the Fick's law, as implemented in COMSOL 4.3, can be written as:

$$\mathbf{\vec{J}_i = -\rho D_i^F\left(\nabla\omega_i + \omega_i\frac{\nabla M}{M}\right)} \tag{16}$$

where D_i^F (cm^2/s) is the diffusion coefficient for each isotope (here assumed to be isotropic) and M (g) is the mass fraction weighted molar mass and is defined as:

$$M = \left(\sum_i \frac{\omega_i}{M_i}\right)^{-1} \tag{17}$$

To find the mixture density, ρ, we use Eq. **10**, and the H_2 diffusivity can be found using [33, p. 391]:

$$D_{H_2} = 1.225 \left(\frac{p_0}{p}\right) \left(\frac{T}{400}\right)^{1.667} \tag{18}$$

where p_0 (atm) is the atmospheric pressure. The diffusivity for the other two isotopes is scaled from that of hydrogen and the respective molecular masses as:

$$D_{D_2} = D_{H_2} \sqrt{\frac{M_{H_2}}{M_{D_2}}} \tag{19}$$

$$D_{HD} = D_{H_2} \sqrt{\frac{M_{H_2}}{M_{HD}}} \tag{20}$$

Finally, in the packed powder bed, the free-stream diffusivities are multiplied by the bed porosity (i.e., in essence D's can be thought of dispersion coefficients, even though tortuosity factor is not included).

2.3. Kinetics

In this section, we describe the kinetics of the isotope exchange by first describing the Reaction and then the Energetics involved in these processes.

Reactions

The general set of exchange reactions (for zero net gas sorption during exchange) is:

$$\mathbf{D_2 + H_s \rightleftarrows HD + D_s} \tag{21}$$

$$\mathbf{HD + H_s \rightleftarrows H_2 + D_s} \tag{22}$$

The isotope exchange is calculated using the technique described by Folz and Melius [28] in terms of a pair of ordinary differential equations for $[H_s]$ and $[D_s]$ as follows:

$$\frac{d[D_S]}{dt} = k_1\left[\widetilde{D_2}\right][H_s] + k_2\left[\widetilde{HD}\right][H_s] - k_{-1}\left[\widetilde{HD}\right][D_s] - k_{-2}\left[\widetilde{H_2}\right][D_s], \tag{23}$$

$$\frac{d[H_S]}{dt} = -\frac{d[D_S]}{dt} \tag{24}$$

In this work the relationships among the various k's are defined as [15]:

$$\frac{k_1}{k_{-1}} = 1.968\exp\left(-\frac{2.73\times10^{10}}{RT}\right), \tag{25}$$

$$\boldsymbol{k_2 = \frac{1}{2}k_1}, \tag{26}$$

$$\boldsymbol{\frac{k_2}{k_{-2}} = 0.561exp\left(-\frac{2.09\times10^{10}}{RT}\right)}. \tag{27}$$

An equation for k_1 is provided in [28] as:

$$\boldsymbol{k_1 = \frac{\nu_t c_f}{2\sqrt{\alpha}N_s}} \tag{28}$$

where ν_t (cm/sec) is the mixture thermal velocity (defined below), c_f is a dimensionless calibration factor that is also referred to as the sticking probability[1] and is on the order of 10^{-7}, α=2.51 is the isotope exchange coefficient [34], and N_s (moles/cm^2) is the surface species concentration, where according to [28] it is defined as: N_s=[H_s]+[D_s]. The mixture thermal velocity is defined as follows:

$$\nu_t = \frac{1}{\rho_g}\left(\left[\widetilde{H_2}\right] + \left[\widetilde{HD}\right]\sqrt{\frac{M_{H_2}}{M_{HD}}} + \left[\widetilde{D_2}\right]\sqrt{\frac{M_{H_2}}{M_{D_2}}}\right)\sqrt{\frac{8RT}{\pi M_{H_2}}} \tag{29}$$

where the term in the radical represents the hydrogen thermal velocity.

Energetics

For the hydrogen dissolution reaction, $H_2+2V_b \leftrightarrows 2H_b$, where the subscript "b" refers to bulk dissolution in moles per unit volume and V_b is a vacancy in the bulk hydride material. Larson et al. [34] derive the equilibrium constant as:

$$\widetilde{K}_H = 2.05\times10^{-4}T\exp\left[\frac{1.0035\times10^{12}-9.004\times10^{11}(x_H+x_D)}{RT}\right] \tag{30}$$

This formulation reflects nonideality corrections where the actual enthalpies for V_b and H_b are

$$H_{V_b} = H^0_{V_b} - 22.51(1-x_V)^2 \tag{31}$$

and

$$H_{H_b} = H^0_{H_b} - 22.51x_V^2 \tag{32}$$

[1]Foltz and Melius use a symbol *p* for this variable.

and x_V is mole fraction of vacancies. (Technically, these refer to the special case in which the cross-coefficient is equal to the nominal value of 45.02.) The standard enthalpy of reaction is derived from the combination of

$$K_H = exp\left(-\frac{\Delta G_H^0}{RT}\right) \tag{33}$$

and the Gibbs-Helmholtz equation

$$\frac{\partial}{\partial T}\left(-\frac{\Delta G_H^0}{T}\right) = -\frac{\Delta H_H^0}{T^2} \tag{34}$$

which yields

$$\boldsymbol{\Delta H_H = -1.0035 \times 10^{12} - 9.004 \times 10^{11}(x_H + x_D)\ (\frac{erg}{mole})} \tag{35}$$

Here, x_H and x_D are the hydrogen and deuterium stoichiometry, respectively. For deuterium dissolution, the empirical equilibrium constant is

$$\widetilde{K}_D = 2.265 \times 10^{-4} T\ exp\left[\frac{9.553\times10^{12} - 9.004\times10^{11}(x_H + x_D)}{RT}\right] \tag{36}$$

From which it follows:

$$\boldsymbol{\Delta H_D = -9.553 \times 10^{11} - 9.004 \times 10^{11}(x_H + x_D)\ (\frac{erg}{mole})} \tag{37}$$

For the full exchange reaction, the heat of reaction is simply the difference between these two equations or:

$$\boldsymbol{\Delta H_e = \Delta H_H - \Delta H_D = -4.82 \times 10^{10}\ (\frac{erg}{mole})} \tag{38}$$

That is the enthalpy of exchange, based on this formulation, is independent of the compositions. We refer to ΔH_e as the solid phase enthalpy change. We should note that while although x_H and x_D are assumed to be constants, we generally assume that x_H and x_D are temperature dependent. We will introduce the formulation for pressure/temperature-dependent stoichiometry later in this work.

For the gas phase reaction, $H_2 + D_2 \leftrightarrows 2HD$, the equilibrium constant is [28, Eq. 15]:

$$K_G = 4.242 exp\left(-\frac{78.096}{RT}\right) \tag{39}$$

so the heat of reaction is simply

$$\Delta H_g^0 = 78.096R = 6.493 \times 10^9\ (\frac{erg}{mole}) \tag{40}$$

Now, for the F&M [28, Eq. 3a] reaction in. 21, the heat of reaction is:

$$\Delta H_{(21)} = 1/2\left(\Delta H_g^0 - \Delta H_H + \Delta H_D\right) = 2.74 \times 10^{10}\ (\frac{erg}{mole}) \tag{41}$$

and for the second reaction 22 [28, Eq. 3b], the heat of reaction is:

$$\Delta H_{(21)} = 1/2\left(-\Delta H_g^0 - \Delta H_H + \Delta H_D\right) = 2.09 \times 10^{10}\ (\frac{erg}{mole}) \tag{42}$$

As a check, note that the sum of Eqs. **Error! Reference source not found.** and **Error! Reference source not found.** is the reverse of the full exchange reaction of the preceding equation and that the heats of reaction relate correspondingly, i.e., Eq. 38.

However, this formulation assumes the effect of H and D concentration is the same, which unlikely given the different stoichiometry between equilibrium PdD_x and PdH_x. To account for the variation between x_H and x_D a normalization factor is formulated based on the stoichiometry differences. As a first guess, the adjusted heats of reaction become:

$$\Delta H_H = -1.0035 \times 10^{12} + 9.004 \times 10^{11}\left(x_H + \frac{2\bar{x}_H}{\bar{x}_H + \bar{x}_D} x_D\right)\ (\frac{ergs}{mole}) \tag{43}$$

$$\Delta H_D = -9.553 \times 10^{11} + 9.004 \times 10^{11}\left(x_D + \frac{2\bar{x}_D}{\bar{x}_H + \bar{x}_D} x_H\right)\ (\frac{ergs}{mole}) \tag{44}$$

where $\bar{x}_H$ and $\bar{x}_D$ are the equilibrium stoichiometric values for PdD_x and PdH_x at a given temperature and pressure the formulation of which are given in section 3.2.

2.4. Heat Transport

Assuming thermal equilibrium of the solid and gas (i.e., single temperature), the equation representing heat transfer in a saturated porous media, can be written as, Kaviany [31, Ch. 10]:

$$\left(\rho C_p\right)_{eq} \frac{\partial T}{\partial t} + \left(\rho C_p\right)_g \vec{u}_g \cdot \nabla T = \nabla \cdot \left(K_{eq} \nabla T\right) + Q \tag{45}$$

where ρ (g/cm^3) is density, C_p (erg/g-K) refers to the constant pressure specific heat capacity, T (K) is the temperature, subscript *eq* and *g* respectively refer to equivalent and gas, K (erg/cm-s-K) is the thermal conductivity, and Q (erg/s-m^3) is the volumetric heat source. The equations for the equivalent (or effective) thermal properties, $(\rho C_p)_{eq}$ and K_{eq}, can be written as:

$$\left(\rho C_p\right)_{eq} = \theta\left(\rho C_p\right)_g + (1-\theta)\left(\rho C_p\right)_s \tag{46}$$

$$K_{eq} = \theta K_g + (1-\theta) K_s \tag{47}$$

where θ is the bed porosity and subscript *s* refers to the porous solid. In this report, by solid, we are referring to palladium particles, with a density of ρ_s=12.023 (g/cm^3).

Gas Specific Heat

We calculate the specific heat of gas mixture as:

$$C_{p,g}(T) = [H_2]\frac{C_{p,H_2}(T)}{M_{H_2}} + [HD]C_{p,HD}(T) + [D_2]C_{p,D_2} \tag{48}$$

where $[H_2]$, $[HD]$, and $[D_2]$ refer to the mole fraction of each isotope, M_{H_2} (kg/mol) is the hydrogen molecular weight, $C_{p,H_2}(T)$ (J/mol-K) is the temperature-dependent molar heat capacity for hydrogen. This is provided as tabular data in COMSOL and was included in the previous version of the model, C_{p,D_2}= 5200 (J/kg-K) is a constant, and $C_{p,HD}(T)$ is an arithmetic average of hydrogen and deuterium specific heats.

Solid Specific Heat

Initially, we assumed the solid (Pd) specific heat to simply be a constant ($C_{p,s}$=244 J/kg-K). However, we have updated the model to include the effect of the hydrogen content in the solid as:

$$\mathrm{C_{p,s}} = \mathrm{C_{p,Pd}} + 4.187(0.03083\mathrm{T} - 2.974)\left[\left(\frac{\mathrm{x_H}}{2}\right)/\mathrm{M_{Pd}}\right] \tag{49}$$

Where $C_{p,Pd}$=244 (J/kg-K), x_H is the exchange stoichiometry (calculated separately and is a function of temperature and pressure), M_{Pd}=106.42 (g/mole) is the molecular weight of the palladium. The term $4.187(0.03083T - 2.974)$ is a linear fit to Mitacek and Aston [35] data.

Hydrogen and/or Deuterium Stoichiometry

In this work, the stoichiometry values for the Pd/H and Pd/D are either constant or vary with pressure and temperature. The specific values and/or forms used for various simulations are discussed in separate sections.

Heat Generation Term, Q

In this work, we define the volumetric power source as the production rate of [HD] (mol/cm^3-s), $\frac{\partial[HD]}{\partial t}$, times its heat of reaction minus the production rates of Pd-D and Pd-H (or $\frac{\partial[D_s]}{\partial t}$) times their heat of reaction or:

$$\mathrm{Q} = \mathrm{S_A}\left[\left(\frac{-\Delta\mathrm{H_g^0}}{2}\right)\dot{\mathrm{H}}\mathrm{D} + \Delta\mathrm{H_e}\frac{\mathrm{d[D_s]}}{\mathrm{dt}}\right], \tag{50}$$

Moreover, ΔH_g^0 and ΔH_e are the gas phase and full exchange heats of reaction, i.e., the enthalpy change for the reactions, which were previously introduced.

3. COMSOL SIMULATIONS RESULTS

In this section we discuss the COMSOL simulations results for a number of cases. Each case, in general, is an attempt to compare COMSOL results to experimental data.

3.1. F&M Reverse Exchange

Our first test of the COMSOL isotope exchange model is the reverse reaction, i.e., H-to-D of Foltz and Melius (F&M) [28]. This case involves injection of D_2 into a tube filled with initially hydrided palladium powder. The model geometry comprised of a 20.3 cm long tube with a diameter of 1 cm. As in the F&M experiment, the tube inlet is subjected to a monotonically increasing pressure of 1124 torr at the start and ending with a pressure of 1128 torr at the end of the simulations. The tube exit was kept at a pressure of 753 torr, which was also the bed initial pressure. The experiment was nominally isothermal with an initial bed temperature of 299 K. Thus, we neglected the effect of heat transfer on the exchange process. The bed stoichiometry is comprised of β-$PdD_{0.61}$ and β-$PdH_{0.65}$. Other relevant parameters are listed in Table 1. Two other permeability values, namely, κ_H and κ_D, where also reported. From Table 1, we can see that these permeability values are a bit larger than those of *Carman-Kozeny*, i.e. Eq. 3 and Eq. 4. So, we decided, in addition to these permeability equations, to also test the effects of κ_H and κ_D on the simulations:

Table 1. Model Parameters For F&M H-to-D Simulations.

Parameter	Value
Particle diameter range, d_p	106–124 μm
Geometric mean, d_p	114.65 μm
Clean specific surface area, S (based on d_p = 114.65 μm)	523.34 cm^{-1} ($6/d_p$)
Hydrided specific surface area, S_0 (based on a 3% reduction)	507.64 cm^{-1} (–3%)
Clean porosity, θ_0	0.38
Hydrided porosity (10.1% expansion), θ	0.31
Hydrided bulk density, $\rho_b=(1-\theta)\,\rho_s$	8.296 g/cm^3
Bed Permeability, based on Eq. **3**	4.86×10^{-8} cm^2
Bed Permeability, based on Eq. 4	3.98×10^{-8} cm^2
Hydrided permeability κ_H	5.4×10^{-8} cm^2
Deuterided permeability κ_D	6.1×10^{-8} cm^2

Since we did not have access to the F&M experimental data, we inserted the image from their report for the H-to-D experiment and simulation. This image is shown in Figure 1. In their simulation of the H-to-D experiment, they used a sticking probability of c_f=2.6×10^{-7} (α=2.4), where we also used the same values in our simulations and did not study the effects of varying them on our results. However, in the final memo of the FY12 work [36], we showed increasing sticking probability, c_f, tends to sharpen the gas partial pressure fronts.

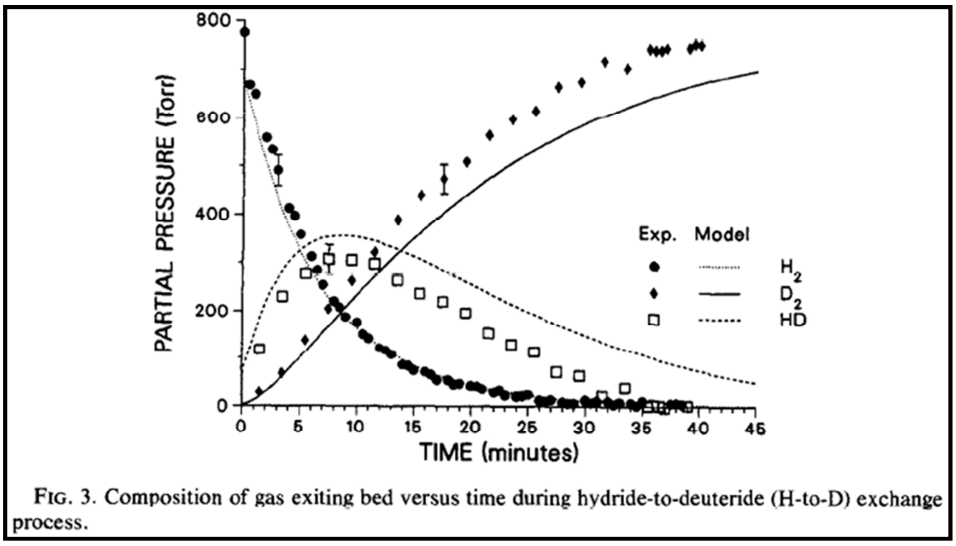

FIG. 3. Composition of gas exiting bed versus time during hydride-to-deuteride (H-to-D) exchange process.

Figure 1: This figure has been copied from Foltz and Melius (1987) paper as the basis to compare their results to those of COMSOL simulations discussed here.

Figure 2 shows the simulated D_2, H_2, and HD partial pressures versus time, at the bed exit. The time and partial pressure axes are set to be same as those shown in Figure 1. However, in our simulations, we show four sets of results, where we have studied the effects of bed permeability on the partial pressures of various isotopes.

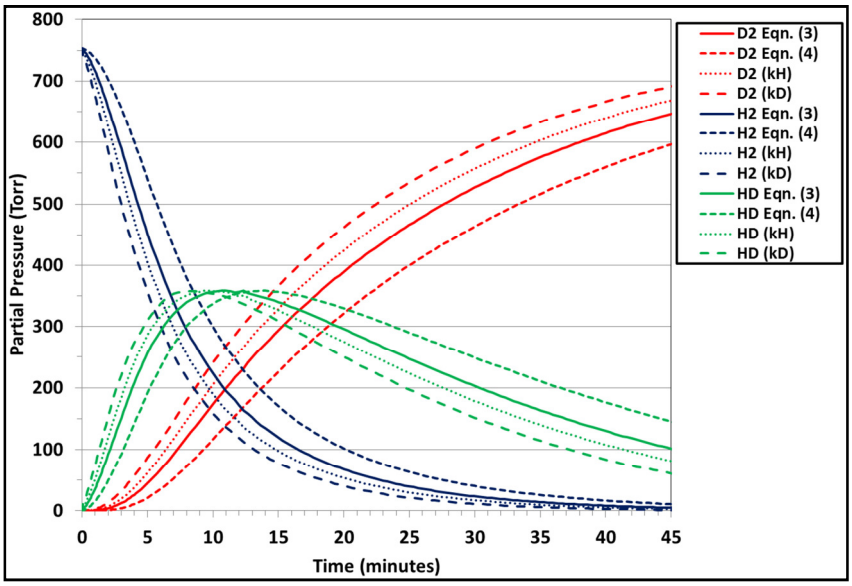

Figure 2: Simulated gas composition at the bed exit versus time for the Foltz and Melius H-to-D exchange experiments, for four different bed permeability models.

The COMSOL results in Figure 2 are clearly comparable to those of F&M in Figure 1.That is, there is sharp decline in the H_2 partial pressure over time, as the D_2 isotope builds up. Moreover, from the experiment the cross-over time for the H→D is at ~200 torr between 8 and 9 minutes.

While the cross-over in our simulations is also at ~200 torr, the time is mainly affected by the choice of permeability model. The earliest cross-over time is directly based on the value of permeability, where we can see in Table 1, κ_D has the largest permeability and Eq. 4 the smallest. In fact using κ_D the cross-over time is at 8.7 min., which is closest to the F&M data. We also note that using κ_D D_2 partial pressure after 45 min. is closest to that of F&M. Finally, the peak HD partial pressure is ~350 torr which is fairly close to the model curves of F&M in Figure 1.

3.2. Recent F&M-like Experiments

A series of forward exchange (i.e., D-to-H) tube experiments, at different temperatures, were recently performed by Steve Rice (08254) and others. These experiments were essentially similar to those of F&M experiments. Steve Rice provided us with isotope mole fraction histories for each experiment, which we use to test our COMSOL model results. The three experiments being simulated here were at temperatures, T=80, 29, and -19 ^{o}C. The parameters common among the three experiments are listed in Table 2.

Table 2: Bed parameters and flow properties for F&M-like experiments

Palladium particle diameter	127-145 μm
Tube length	20.3 cm
Tube ID	0.459 cm
Tube OD	0.635 cm
Tube Material	316 ss
Pd Mass	18.83g
Inlet Pressure	~40 psi
Outlet Pressure	~39 psi
Flow rate	0.0564 slpm (0.94 cm^3/sec.)

For all cases, we assumed a particle diameter of 138 μm. Based on the Pd mass and the standard density for Pd, we estimated a bed porosity of θ=0.53. Additionally, we assumed isothermal condition for all cases.

Steve Rice also provided us with an equation to calculate the stoichiometry of the palladium for these particular cases. The suggested equation is as follows:

$$ln\left(\frac{p}{1\ atm}\right) = A - \frac{B-Cx}{T} + DT \tag{51}$$

Where p (atm) is the pressure, A, B, and C are constants are listed below, and x represents the H(D)/Pd atomic molar ratio (i.e., the stoichiometry).

Table 3: Constants for Eq. 51 to calculate the temperature and pressure dependent stoichiometry for Pd-H and Pd-D.

Constant	Pd-H	Pd-D
A	5.830	32.39
B	12640 K	15313 K
C	12832 K	12832 K
D	0.01853 K^{-1}	-0.03127 K^{-1}

Using Eq. 51 and the constants listed above and assuming a pressure of 40 psi (~2.722 atm), we calculated the following stoichiometry values:

Table 4: Resulting stoichiometries for Pd-H and Pd-D at 40 psi for various temperatures.

T (^{o}C)	T (K)	Pd-H ($\bar{x}_H$)	Pd-D ($\bar{x}_D$)
-19	254.15	0.796	0.729
29	302.15	0.739	0.677
80	353.15	0.672	0.633

Finally, it is worth mentioning that in our model, we define $N_s = \left(\bar{x}_D / M_{Pd}\right)(1-\theta)\rho_{Pd}$, making N_s a constant, when $\bar{x}_D$ is also a constant. However, when $\bar{x}_D(T)$, as in Eq. 51, N_s will then vary with temperature as well.

3.2.1. T=80 ^{o}C

Our previous experience with the F&M model was that the two major parameters controlling the solution are the bed permeability, κ, and the sticking probability, c_f (parameter p in [28]). Using bed porosity of θ=0.53 along with the lower and upper particle sizes of 127 and 145 μm, respectively, the corresponding bed permeability values, using Eqs. 3 and 4, become κ=6.26x10^{-7} and κ=8.17x10^{-7} (cm^2), respectively. For our first test of the model, we set particle size to 138 μm, yielding, κ=7.4x10^{-7} (cm^2). Using this κ value and the sticking probability, p_f=2.6x10^{-7} (i.e., the same value as the one used in F&M test). While keeping the bed isothermal, we noticed that the simulated isotope exchange (i.e., D-to-H) completes in less than 100-200 sec., which is much earlier than the experimental data. Based on our experience simulating the earlier F&M simulations, this response indicated to us that perhaps the bed permeability is too large. So, we decided to scale the bed permeability. Figure 3 compares several simulated D_2 mole fraction histories (at the tube exit) to that of experimental data. In this figure, p_f and c_f refer to factor (constant multipliers) for the bed permeability and sticking probability, respectively, we can see that a p_f=0.14 (κ=1.04x10^{-7} (cm^2)), results in a relatively good match of the data. We can see from the figure that the experimental D_2 mole fraction is not initially at 1.0 (mainly because we

are not modeling the long inlet and outlet tubes[2]) and we made no attempt to either adjust our simulation or the data for a match. Decreasing and increasing the p_f values to 0.13 (κ=9.62x10^{-8} (cm^2)) and 0.15 (κ=1.11x10^{-7} (cm^2)), respectively, results in either later or earlier decline in D_2 over time.

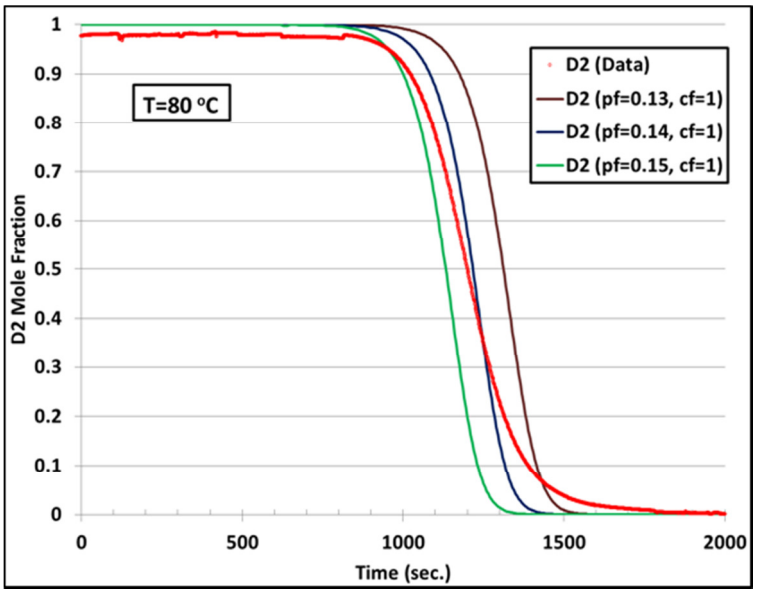

Figure 3: Comparisons of simulated and experimental D_2 mole fraction histories for the 80 °C experiment, depicting the effects of p_f on simulations. For the simulated results p_f and c_f refer to constant multiplier for the bed permeability and sticking probability.

Next, we tested the effects of c_f (i.e., sticking probability) on our simulations, where we decreased and increased this parameter by 25%, respectively. The simulations results along with the experimental data are displayed in Figure 4. We should note that based on the results in Figure 3, chose p_f=0.14. As we mentioned earlier, increasing c_f generally tends to sharpen the exchange curve (i.e., steeper slope), while decreasing it results in a shallower slope. This effect can be seen for the small range of variation used for c_f, where a slightly smaller c_f=0.75 (p~2x10^{-7}) results in a better match of the experimental data during the early phase of exchange. However the rate of D_2 depletion (after ~1,300 sec.), is slower than those of simulations.

Choosing p_f=0.14 and c_f=0.75, Figure 5 compares the simulated and experimental mole fraction for all three isotopes. Considering the time at which HD mole fraction peaks (i.e., D_2 and H_2 curves cross over), before this peak time the data and simulation compare fairly well, even though the simulated peak HD mole fraction is ~13% larger than the experiment. Moreover, the cross-over time is ~1270 sec. for the experiment and 1275 sec. for the simulation. After this time simulated HD and H_2 drop and rise, respectively, fairly quickly, but the experimental data shows

[2] We modeled the inlet and outlet tube using 3 cm long tubes attached to the Pd bed, filled with clear fluid. The pressure drop in the clear fluid (gas) was simulated using Darcy equation, as using Navier-Stokes did not make much of a difference.

a wider distribution. These differences could be due to variability in bed permeability over time or other mechanisms that our model is not currently considering.

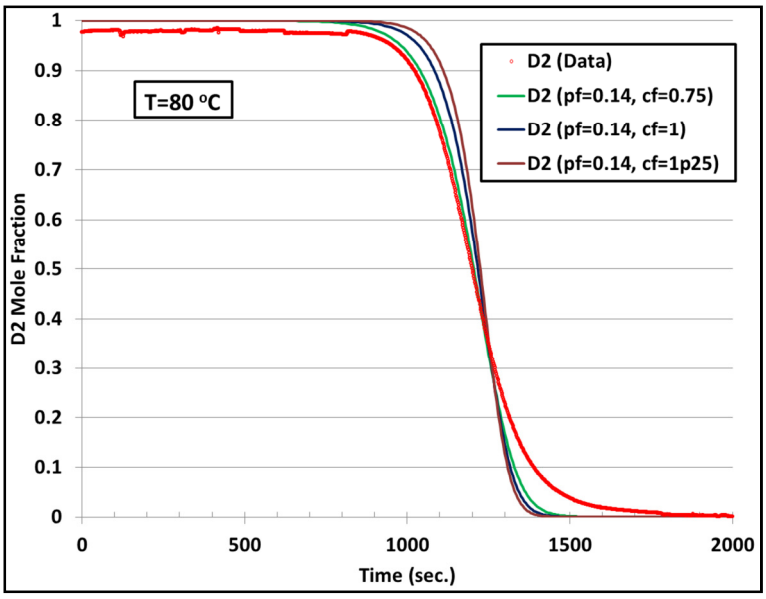

Figure 4: Comparisons of simulated and experimental D_2 mole fraction histories for the 80 °C experiment, depicting the effects of c_f on simulations. For the simulated results p_f and c_f refer to constant multiplier for the bed permeability and sticking probability.

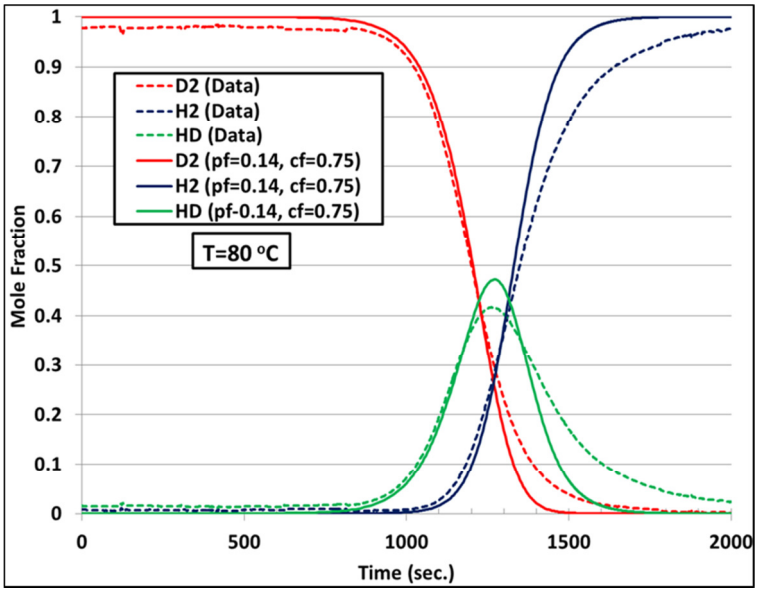

Figure 5: Comparisons of simulated and experimental D_2, H_2, and HD mole fractions histories for the 80 °C experiment. For the simulated results p_f and c_f refer to constant multiplier for the bed permeability and sticking probability.

3.2.2. T=29 °C

Next, we simulated the 29 °C experiments. Since the flow conditions for this experiment were the same as the previous case, in our model we only changed the temperature and the Pd/H and Pd/D constants and essentially repeated the simulations. Experimental data (e.g., see Figure 6) showed that the lowering the experiment's temperature results in quicker drop-off in the D_2 mole fraction history. After a number of test simulations, we decided to use p_f=0.1 (k=7.4x10^{-8} (cm^2)) and study the effects of c_f on the simulations. These results are depicted in Figure 6. We can see that using c_f=1, as was used for the T=80 °C cases, results in D_2 mole fraction remaining near the maximum values of 1.0 for a relatively long period of time, while the data shows D_2 begins to decline fairly quickly. Accordingly, reducing c_f down to 0.1, the simulated breakthrough curve is closer to that of the experiments. However, the simulation shows a faster decline in D_2 history than does the experiment.

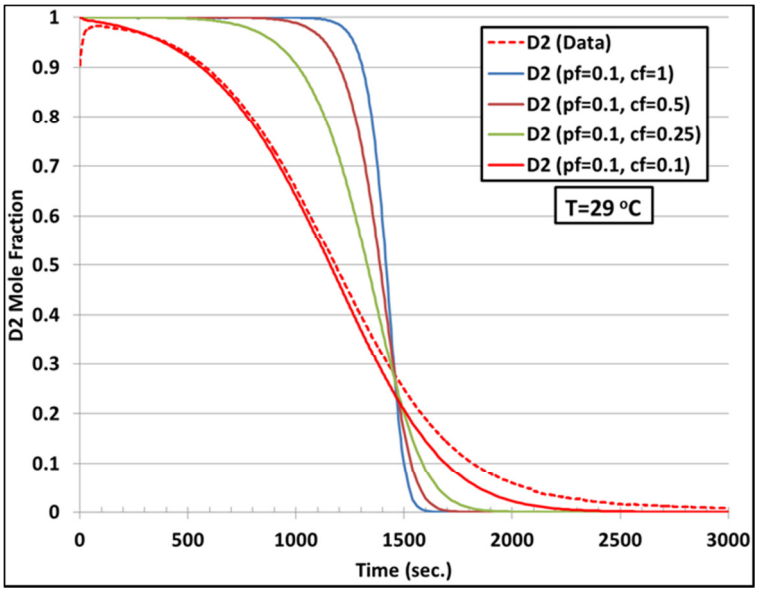

Figure 6: Comparisons of simulated and experimental D_2 mole fraction histories for the 29 °C experiment, depicting the effects of c_f on simulations. For the simulated results p_f and c_f refer to constant multiplier for the bed permeability and sticking probability.

To illustrate the effects of bed permeability, Figure 7 shows that decreasing or increasing p_f by 25%, results in fairly big differences between the simulations and the experimental data. Figure 8 shows the simulated fits to the experimental data for all three isotopes, using p_f =0.1 and c_f =0.1. The predicted peak HD mole fraction is a little less than 10% larger than that of the experiments. In addition, this peak time, which is also the time when D_2 and H_2 curves cross, occurs earlier in the simulation (1,425 sec.) than does in the experiment (~1,445 sec.). We can also see other differences in the H_2 and HD curves. Nevertheless, we did not attempt to get a better fit between the simulation and the experiment, since there are other uncertainties in our model that need to be first addressed before attempting to reduce the difference in simulation with the experiment.

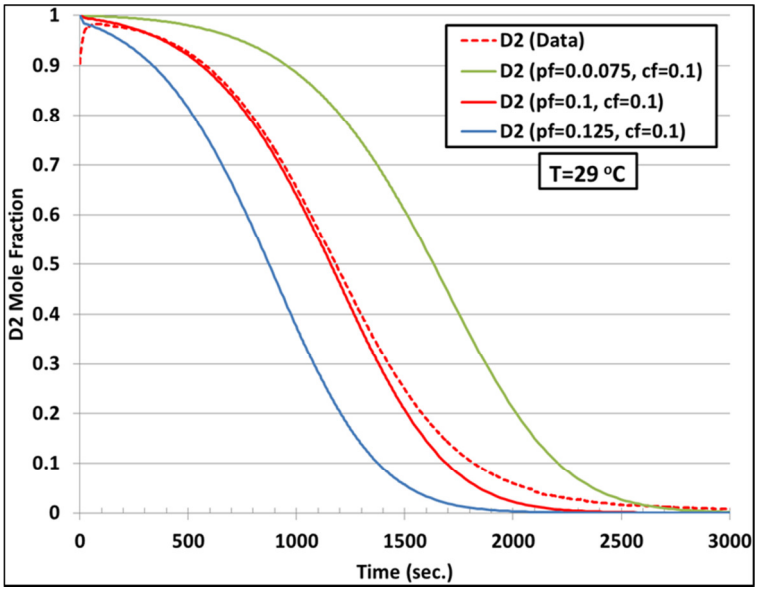

Figure 7: Comparisons of simulated and experimental D_2 mole fraction histories for the 29 °C experiment, depicting the effects of p_f on simulations. For the simulated results p_f and c_f refer to constant multiplier for the bed permeability and sticking probability.

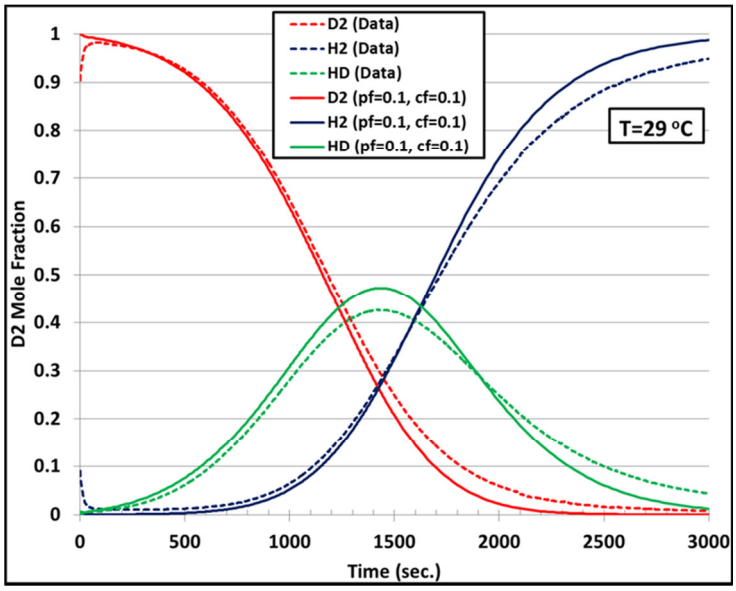

Figure 8: Comparisons of simulated and experimental D_2, H_2, and HD mole fractions histories for the 29 °C experiment. For the simulated results p_f and c_f refer to constant multiplier for the bed permeability and sticking probability.

3.2.3. T=-19 °C

Our final case for these series of simulations is a relatively low temperature experiment (T=-19 °C). This was a much tougher case, trying to match the simulation with the experiment. Experimental data illustrated a fairly rapid drop in D_2. That is, the exchange occurs almost

instantaneously where H_2 begin to build up. Moreover, the initial D_2 mole fraction was closer to 0.63 as opposed to 1.0. Based on our experience from the previous two cases, we decided to consider even smaller p_f and c_f values. Figure 9 compares the experimental D_2 history for c_f =0.01 (i.e. , p=2.6x10^{-8}) and three different p_f values. Clearly, the best match between the data and simulation is for p_f =0.05 and c_f =0.01. For this parameters combinations the overall shape and slope of the simulated D_2 curve is fairly close to the experiments. Moreover, the simulation initially has mole fraction of 1.0, which drops fairly quickly. As an aside, we also tried setting the initial D_2 mole fraction to be close to that of the data, but that did not make a difference with respect to the long term response of the mole fraction history.

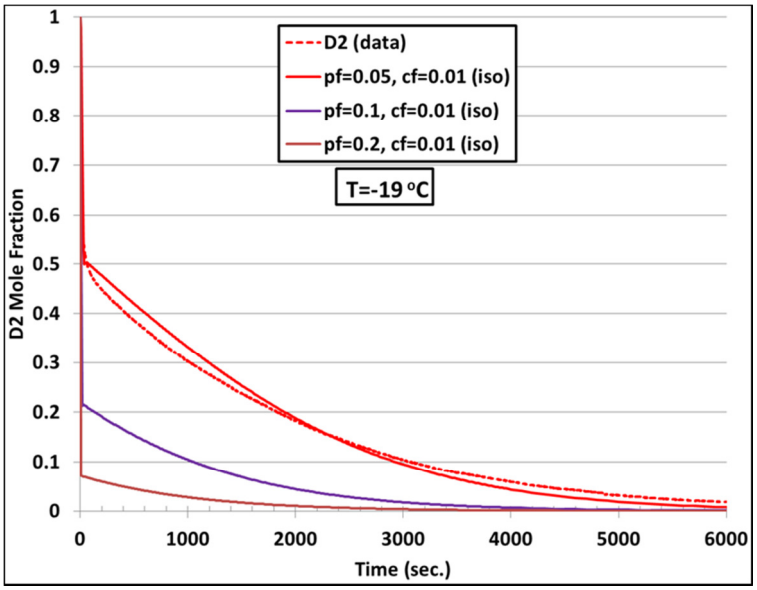

Figure 9: Comparisons of simulated and experimental D_2 mole fraction for the -19 °C experiment, depicting the effects of p_f on simulations. For the simulated results p_f and c_f refer to constant multiplier for the bed permeability and sticking probability.

Figure 10 shows the simulated mole fraction histories for the three isotopes, along with the experimental data. It is obvious that even though we have a relatively good fit for the D_2, the fits for the other two isotopes are fairly poor. In fact, while H_2 is under-predicted, the simulated HD over-predicts the data. We must note that we were able to get better fit for the H_2, using p_f =0.1, however, as shown in Figure 9, this p_f value results in fairly poor D_2 fit.

Since the kinetic reaction rates, k_{-1} and k_{-2} are temperature-dependent, next we decided to examine the effects of using constant k_{-1} and k_{-2}, where we let $k_2=\lambda k_1$, $k_{-1}=\lambda\alpha k_1$, and $k_{-2}=\alpha k_1$, where λ=1.81 and now let α=2.51. The results for this simulation, using the same p_f and c_f values as in Figure 10, are displayed in Figure 11. We now see a slightly better match for the HD and also towards the end of the simulation H_2 mole fraction is a lot closer to the experiment. However, the D_2 fit is no longer as good. Although we were able to improve the D_2 fit using p_f =0.075, but then H_2 is somewhat over-predicted. We think it might be a better idea to use the constant reaction rates for the lower temperature experiments.

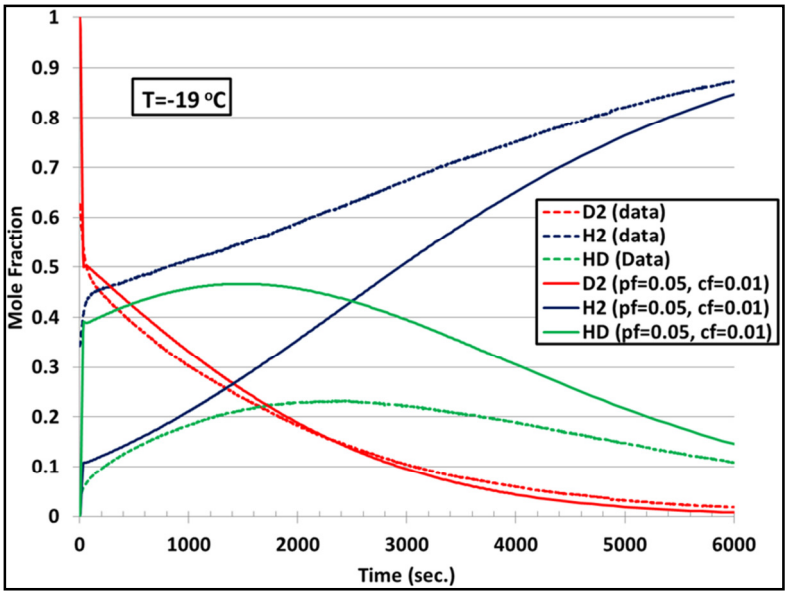

Figure 10: Comparisons of simulated and experimental D_2, H_2, and HD mole fractions histories for the -19 °C experiment. For the simulated results p_f and c_f refer to constant multiplier for the bed permeability and sticking probability.

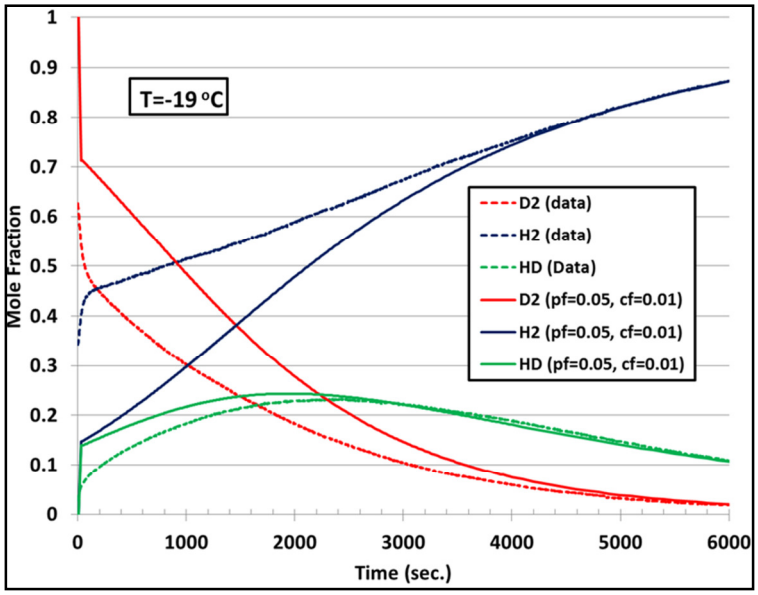

Figure 11: Comparisons of simulated and experimental D_2, H_2, and HD mole fractions histories for the -19 °C experiment. Here the kinetic reaction rates k_2, k_{-1}, and k_{-2} are constant as described in the text.

3.3. Simulations of NENG-7 Experiments

A photograph of one of NENG-7 experiments is shown in Figure 12. Frost is evident as this was a picture from a cryogenic run. This experimental setup is such that it much more thoroughly exercises the COMSOL model. Specifically, its geometry and time scale result in a notably large

thermal response in the Pd bed. Furthermore, as it is a blowdown experiment, there is a highly variable pressure and temperature inlet boundary condition and the whole exchange is completed in well under 5 seconds (as opposed to 1500 s for the F&M experiment).

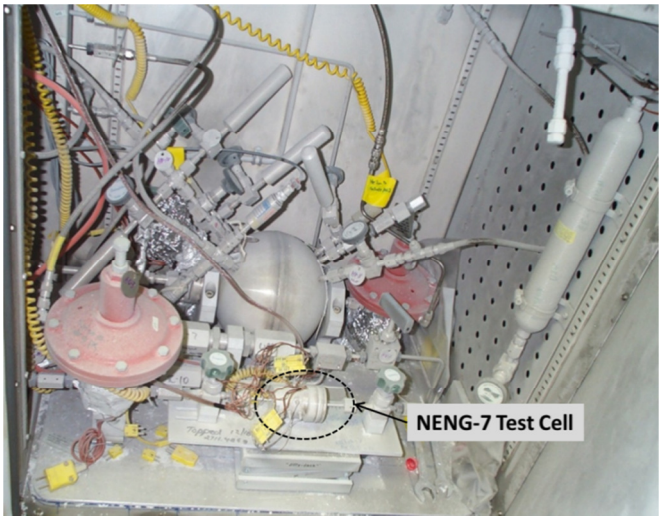

Figure 12: Photograph of the NENG-7 experimental setup.

3.3.1. NENG-7 Boundary Conditions

The flow boundary conditions included time dependent pressures at the inlet and outlet boundaries (see Figure 13) and primarily consisted of the same values as those of NENG-7 experiment and fitted to NETFLOW. Note that while the pressures in this figure are in psi, in our model the unit for pressure is barye. For the heat equation, the inlet boundary also used the same time dependent temperature as that of NENG-7 experiment and was previously fitted by the NETFLOW model (Figure 14) and the outlet bed boundary has a zero heat flux.

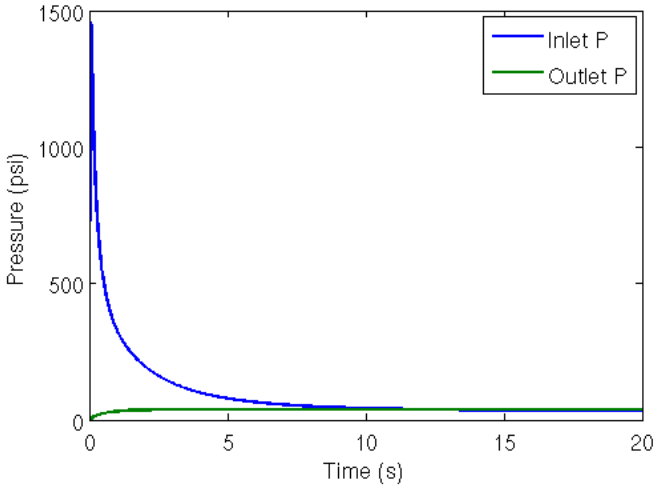

Figure 13: Inlet (left vertical axis) and outlet (right vertical axis) time-dependent pressure boundary conditions used in COMSOL modeling of NENG7 experiments.

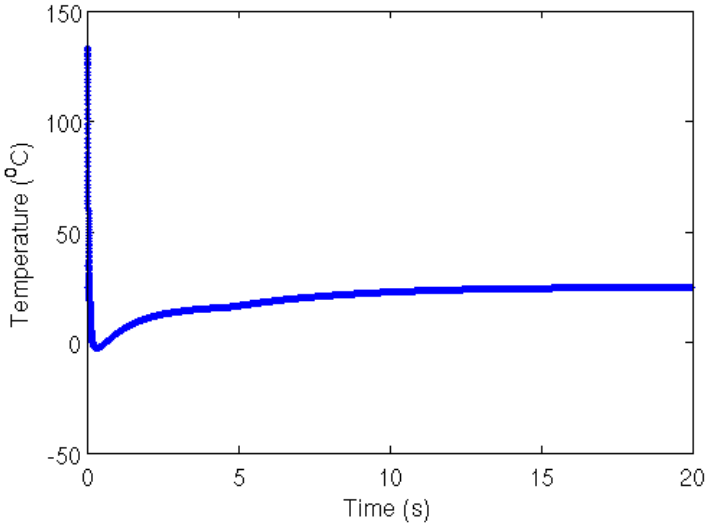

Figure 14: Inlet time-dependent temperature boundary condition used in COMSOL modeling of NENG7 experiments.

3.3.2. Model Geometry

Our COMSOL model of NENG-7 simulations is presented in Figure 15. The model geometry is 2D axi-symmetric and is comprised of 1.778 cm in radius and 3.53 cm long Pd bed. To mimic the heat sink, we have surrounded the bed with a layer of stainless steel.

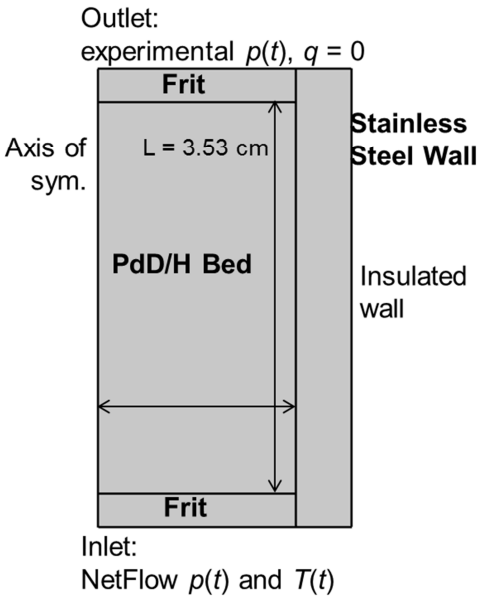

Figure 15: 2D axis-symmetric simplified model of NENG-7 experiments for COMOSOL simulations.

The bed mass 102 grams with a porosity of θ=0.75, with particle specific surface of S_A=3,3063.25 cm^{-1} (i.e., a bed specific surface area of 1,100 m^2/kg). The mesh is comprised of 3,226 quadrilateral elements that are uniform having a size of 0.05 cm.

3.3.3. NENG-7-7 Experimental Comparison

In this section, we discuss the results for a series of COMSOL simulations to predict the data from NENG-7 experiments. Since these experiments were performed under non-isothermal conditions, the temperature histories for number of thermocouple locations are available. Moreover, we were also provided with the experimental mole fraction histories for the three species. We start with treating the bed as isothermal.

Isothermal Simulations

To remove the uncertainties associated with our inlet temperature boundary condition as well as the various thermals (bed and gas) properties, we first considered the bed to be at a constant temperature of 28 ^oC. Figure 16 compares the mole fraction histories for the three isotopes, at the midpoint of the bed exit, for the COMSOL simulation and experimental data. Although we performed a series of simulations where we varied the bed permeability and the sticking probability, here we are showing the results for one of the cases where the simulation and data compare relatively good. For this case, bed permeability, κ=2.68x10^{-10} cm^2 and the sticking probability, c_f=5.2x10^{-7}. We can see that for this choice of κ and c_f combinations, D_2 decline starts a bit later than what the experiment shows which naturally result in H_2 build up to be later.

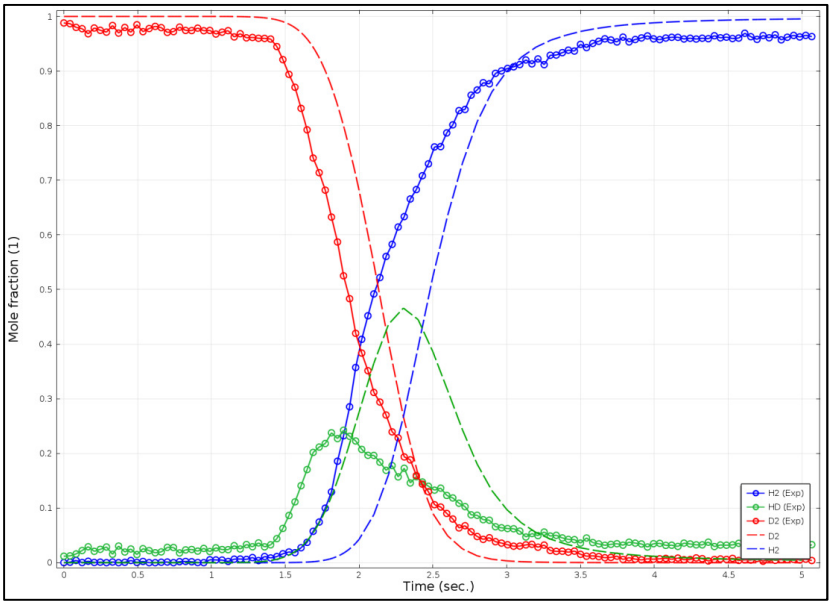

Figure 16: Comparisons of the simulated (dashed curves) and experimental (solid curves with circles) mole fraction histories at the bed exit, under isothermal condition.

As previously discussed, the sticking probability, c_f, tends to control how sharp the isotope exchange curves are. To illustrate this, Figure 17 shows the mole fraction histories for a using κ=2.72x10^{-10} cm^2 and c_f=2.6x10^{-7}, 5.2x10^{-7}, and 7.8x10^{-7}. Examining the HD curves, as c_f increases, there is a smaller spread of the HD isotope, which also affects the shape if the curves for the other two isotopes. It is interesting that if the sticking probability temporally varies, we might be able to obtain a better match of the experimental data.

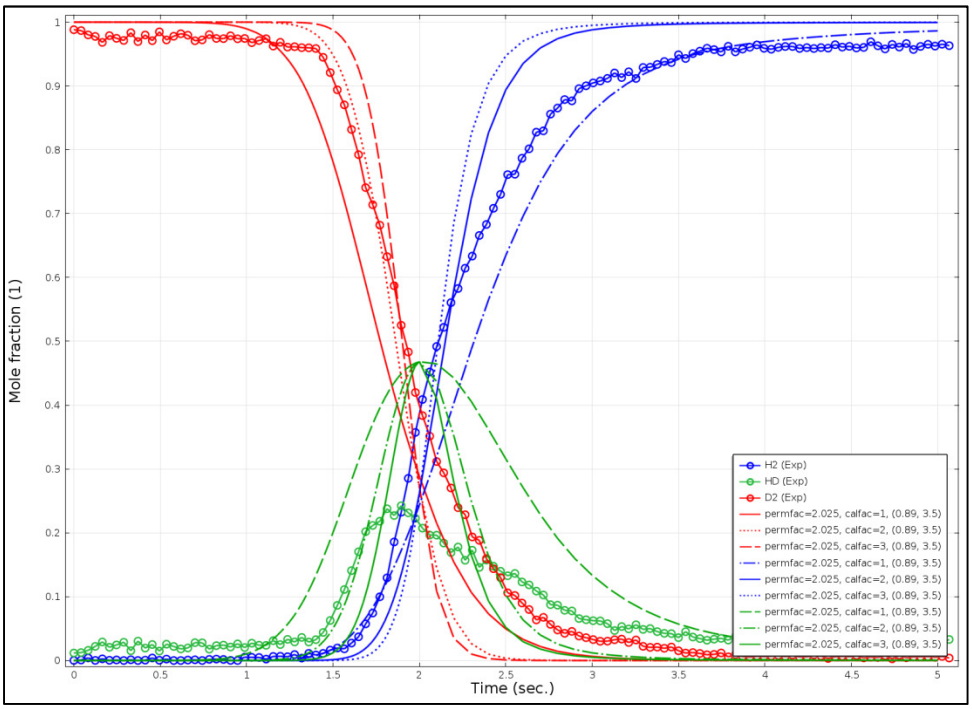

Figure 17: Comparisons of the simulated and experimental (solid curves with circles) mole fraction histories at the bed exit, under isothermal condition, for various sticking probability values.

Non-isothermal Simulations

It is known that the packing process causes the particle density and thus permeability of the bed vary axially and radially. This causes the flow through the bed to vary radial and produces a curved reaction front observed from neutron radiography measurements provided to us. Figure 18 shows one of these measurements for a similar type of experiment. The dark area is the reacted region and the lighter area is the region that has not yet reacted.

Figure 18: Neutron radiography image of room temperature palladium hydride isotope exchange experiment showing the curved reaction front.

As a first attempt to account for the variable particle density, we apply Eqs. 5 and 6 to the bed permeability with values for b_1 and b_2 of 1.3 and 1.15. In the following cases, we use the gas specific heat from Eq. 46 and the heat generation from Eqs. 43 and 44. The fitting parameters p_f and c_f are set to 3.5 and 2.75, respectively. To address the continued issue with temperature, we vary the bed thermal conductivity to see the effect on the temperature and reaction front curvature. Figure 19 shows the reaction front at a time of 1 s for the cases with uniform and non-uniform bed permeability and various thermal conductivities. Varying the thermal conductivities allows us to examine the lack of agreement with the temperature at all thermal couples and allows us to see how the greater spread of heat affects the reaction front.

For the case with uniform bed permeability (Figure 19-A), the reaction front is not flat, but instead reacts faster at the outer wall. This is due to higher temperatures in the center of the bed causing the gas to expand and pushing the flow more towards the outer wall. The effect is greater at lower thermal conductivities since the temperature variation radially is greater for a lower thermal conductivity.

For the case with non-uniform bed permeability, three thermal conductivities for the porous bed are examined: K_{eq} the conductivity based on effective medium theory from Eq. 45 (Figure 19-B), four times K_{eq} (Figure 19-C), and ten times K_{eq} (Figure 19-D). As the thermal conductivity is increased, the flow to the outer wall is reduced since the radial temperature gradient is reduced. Additionally, the non-uniform bed permeability reduces the permeability and thus flow at the outer wall causing a reaction front that is faster in the center of the bed.

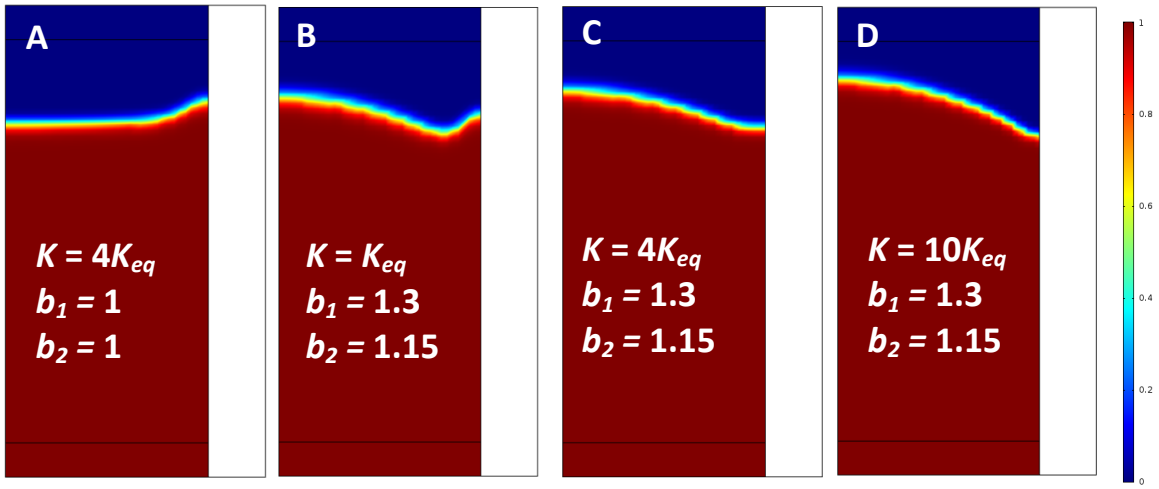

Figure 19: D_2 mass fractions showing the reaction front curvatures 1 s into the reaction for uniform and non-uniform bed permeability at various thermal conductivities.

The temperature histories for case (A) the uniform bed permeability with 4 times K_{eq} and non-uniform bed permeability cases (B) with conductivities of K_{eq} and (C) with 4 times K_{eq} for the first center thermocouple (TC5) are plotted in Figure 20. Case (A) shows a maximum temperature similar to the measurement data, but reaches that temperature faster and the temperature decays faster. However, this case does not have the expected reaction front curvature. Case (B) reaches a much higher maximum temperature, though at a similar time, and the temperature decays more slowly. This case also does not have the expected reaction front profile, though it is better that case (A). Case (C) has a slightly lower maximum temperature and reaches that temperature earlier and the temperature decays more quickly. This case also shows a double peak, which may not be observable on a thermocouple. This case has closer to the expected reaction front profile. The later temperature peak between cases (A) and (C) is caused by the reduced centerline permeability in case (C) to keep the average permeability constant between the cases. The later temperature peak between cases (C) and (B) is due to the lower thermal conductivity increasing the time it takes for heat to transfer axially to the position of the thermocouple. These results lead us to believe there may be an issue with the heat transfer in our model reducing the axial/radial heat flow. This may be caused by the use of a one temperature model that assumes the gas and solid in the porous region has the same temperature at any given point.

The predicted mass fraction time histories for cases (A), (B), and (C) are plotted in Figure 21. We can now see how the radial variation in temperature and non-uniform bed permeability cause assymetry in the mass fraction time histories. Cases (B) and (C) show more similarity with the data and case (C) is plotted with the data in Figure 22. This figure shows a good agreement with the data, which can likely be tuned to fit better.

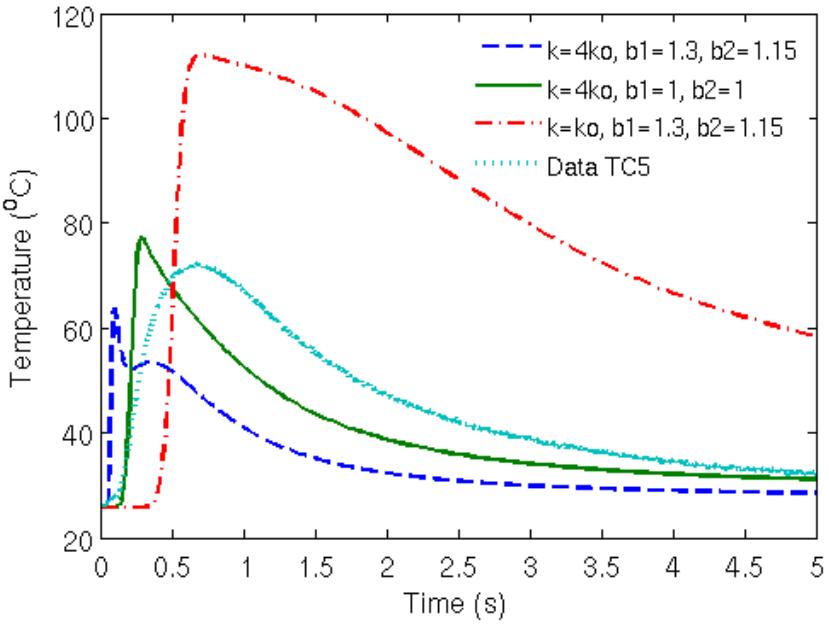

Figure 20: The measured and predicted temperature histories for case (A) the uniform bed permeability with 4 times K_{eq} and non-uniform bed permeability cases (B) with conductivity of K_{eq} and (C) with 4 times K_{eq} for the center thermocouple (TC5) are plotted.

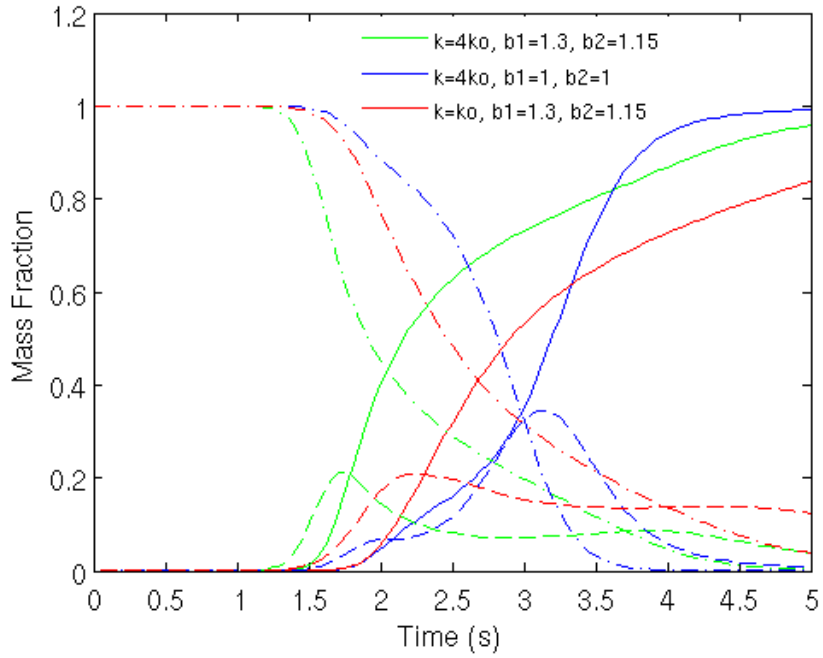

Figure 21: The predicted exit mass fraction histories for case (A) the uniform bed permeability with 4 times K_{eq} and non-uniform bed permeability cases (B) with conductivities of K_{eq} and (C) with 4 times K_{eq}.

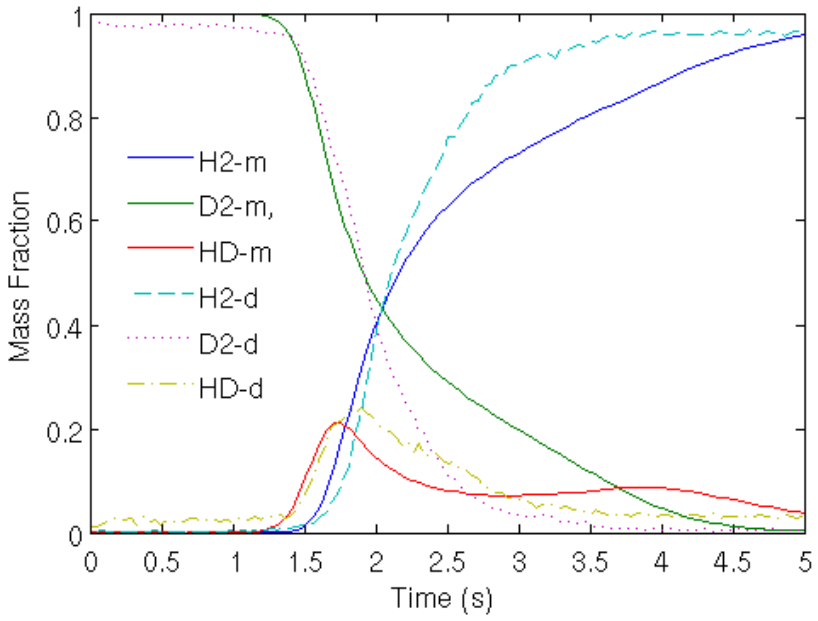

Figure 22: The measured and predicted exit mass fraction histories for case (C) the non-uniform bed permeability with thermal conductivity 4 times K_{eq}.

The predicted temperature histories for case (C) are plotted along with the measured data for each thermocouple location along the centerline (Figure 23) and along the outer wall (Figure 24). It is interesting to note that the two thermocouples halfway and three quarters of the way through the bed length do not show the same decay as the thermocouple one quarter of the way through the bed length both in the center and outer wall location. This is likely due to the inlet gas cooling the beginning of the bed and the bed heating the gas so that later in the bed the cooling effects of the gas are much reduced. For this case, our model is not properly accounting for this effect. Our model is showing the highest peak temperature at the mid-length position and earlier peaking times for all locations. For this case, the temperatures at the center line still show higher peak values and the temperatures at the outer wall show lower peak values. Although the temperature histories are not too far off, there is still much room for improvement. However, the discrepancies in the temperatures seem to only have a small effect on the mass fraction output, which is the quantity of interest for these systems.

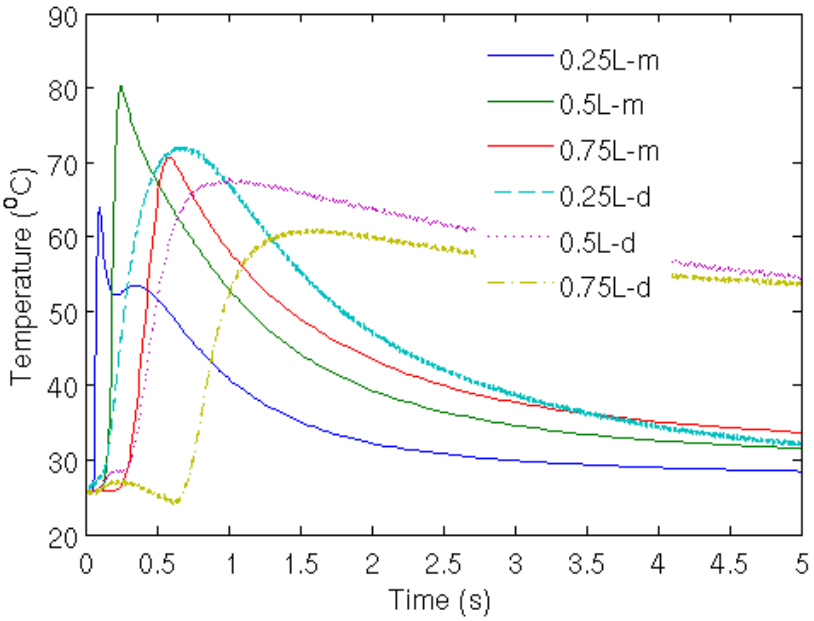

Figure 23: The measured and predicted temperature histories for case (C) along the centerline for the three thermocouple locations.

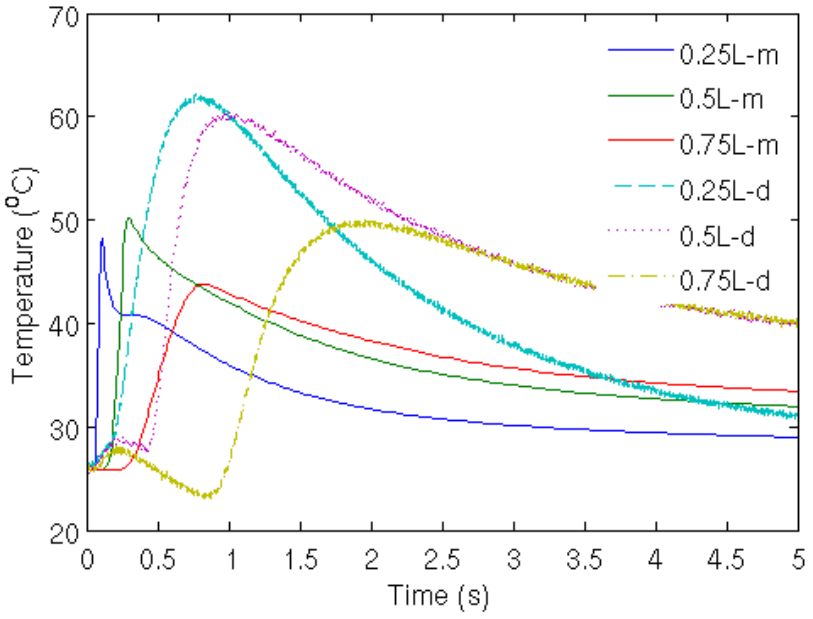

Figure 24: The measured and predicted temperature histories for case (C) along the outer wall for the three thermocouple locations.

No Reaction Flow Through Study

In an effort to better understand the issues with the temperature histories, case (C) with no reaction is compared to temperature data from a H_2 flow through test on a PdH bed. NENG-7-12-CO experiment involved passing H_2 through a NENG7 bed where the bed started out with "almost" pure H_2. The experiment would then involve heat released as a result of pressure change from the H_2 supply followed by the subsequent pressure drop and cooling of the bed. In this work, we use the experimental temperature histories at various thermocouple locations to test our COMSOL model, when there is isotope exchange.

The experimental temperature histories at various thermocouple (TC) locations are shown in Figure 25 and Figure 26. Thermocouples TC1, TC3, and TC5 are located along the bed axis of symmetry at ¾, ½, and ¼ locations along the bed height, respectively (Figure 25). Thermocouples TC2, TC4, and TC6 are located near the right boundary of the bed at ¾, ½, and ¼ locations along the bed height, respectively (Figure 26).

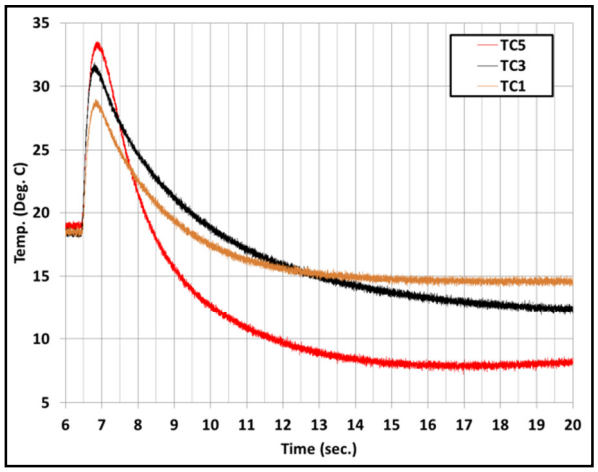

Figure 25: NENG-7-12-CO Thermocouple temperature histories at various locations in the bed: TC5, TC3, and TC1 represent thermocouples on the bed axis of symmetry at 1/4, 1/2, and 3/4 along the bed height.

From these figures, we can see that temperature rise at various thermocouple locations is between ~9 to 14 ^{o}C (that is from an average initial temperature of ~19 ^{o}C to a peak temperature of ~33 ^{o}C). Moreover, while we see slightly more variations in the peak temperature among TC5, TC3, and TC1, the variations among the thermocouples on near outer boundary of the bed (i.e., TC2, TC4, and TC6) is less. Although the long-term temperature drop for TC5 is greatest among all other thermocouples, the other thermocouples appear to settle around 14-16 ^{o}C. This response indicates to us that the bed is heating up and cooling off fairly uniformly. Another interesting observation is that the temperature rise for all thermocouples is nearly the same. That is, as though there was no delay in the bed heating and the entire bed started to heat up almost instantaneously. Closer inspection of the data indicated that the rise time differences among the various thermocouples were relatively small, i.e., for all practical purpose the rise times were nearly the same.

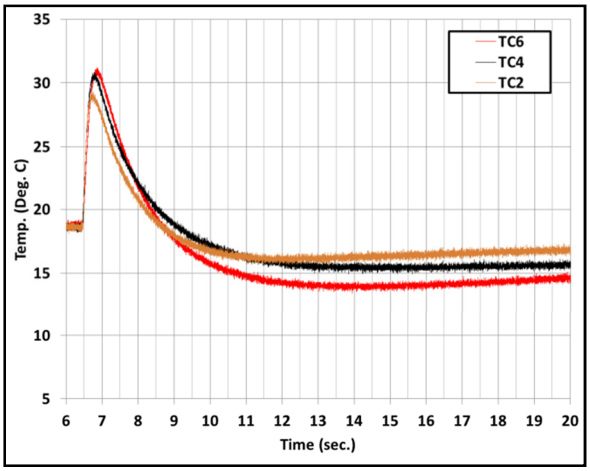

Figure 26: NENG-7-12-CO Thermocouple temperature histories at various locations in the bed: TC6, TC4, and TC2 represent thermocouples near the bed right boundary at 1/4, 1/2, and 3/4 along the bed height.

The measured and predicted temperature histories are plotted in Figs. 27 and 28 for the centerline and outer wall thermocouples, respectively. For this case, we now see a longer temperature ramp up and decay in the model rather than in the measurement as was seen before. Additionally, the measured temperature histories are very similar between all the thermocouples, while there are significant differences in the modeled temperatures at these locations. Finally, the boundary conditions applied to this case do not seem to be the same given that the temperatures the thermocouples are decaying to is significantly lower than that in the model.

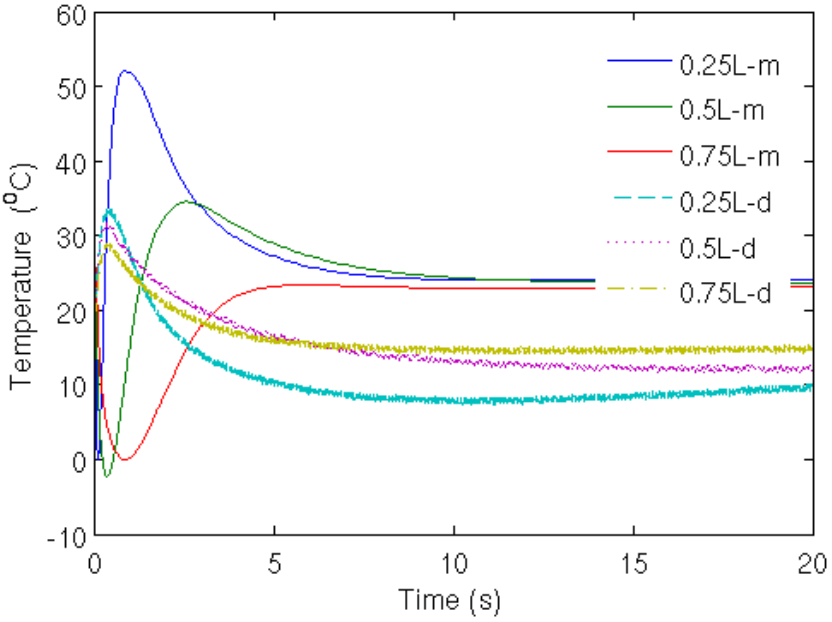

Figure 27: The measured and predicted temperature histories for case (C) with no reaction along the centerline for the three thermocouple locations.

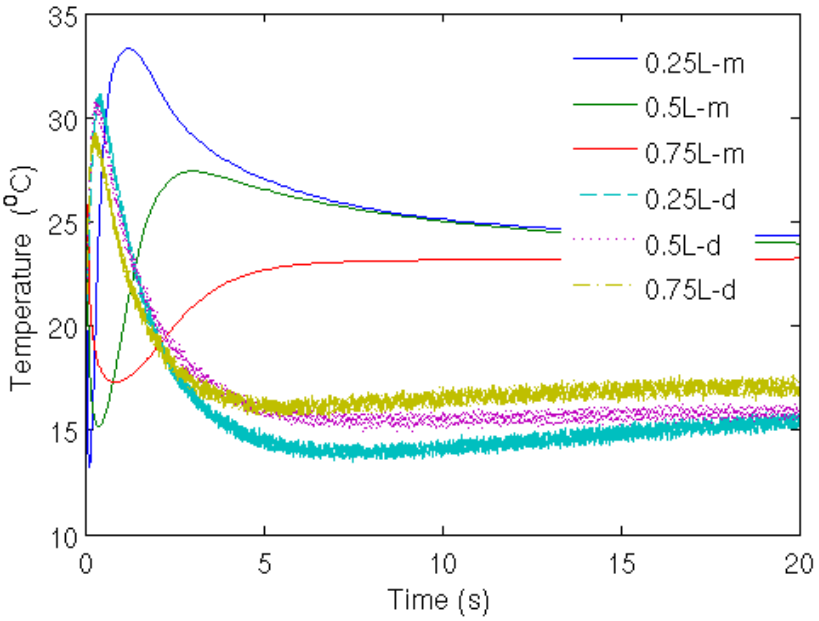

Figure 28: The measured and predicted temperature histories for case (C) with no reaction along the outer wall for the three thermocouple locations.

4. CONCLUSIONS

Sandia researchers have implemented a palladium hydride isotope exchange simulation to account for previously inaccessible multi-dimensional effects. The multiphysics 2D axi-symmetric model simulates the temperature and pressure dependent exchange reaction kinetics, pressure and isotope dependent stoichiometry, heat generation from the reaction, reacting gas flow through porous media, and non-uniformities in the bed permeability. The new model is now able to replicate the curved reaction front and asymmetry of the exit gas mass fractions over time. The improved understanding of the exchange process and its dependence on the non-uniform bed properties and temperatures in these larger systems is critical to the future design of such systems. Improvements are still needed to correctly model the temperature histories across the entire particle bed, but comparisons of the quantity of interest, mass fraction output of the gases, are promising in their agreements with the measurements.

5. REFERENCES

1 Alefeld, G., *Phase transitions of hydrogen in metals due to elastic interaction.* Berichte der Bunsen-Gesellschaft Physikal Chemie, 1972. **76**(8): p. 746-755.

2 Völkl, J. and G. Alefeld, *Diffusion of Hydrogen in Metals*, in *Diffusion in Solids, Recent Developments*, A.S. Nowick and J.J. Burton, Editors. 1975, Academic Press: New York, NY. p. 321-348.

3 Lässer, R. and K.-H. Klatt, *Solubility of hydrogen isotopes in palladium.* Physical Review B, 1983. **28**(2): p. 748-758.

4 Thomas, G.J., *Hydrogen trapping in FCC metals*, 1980, Sandia National Laboratories: Albuquerque, NM. p. 22.

5 Scholten, J.J.F. and J.A. Konvalinka, *Hydrogen-deuterium equilibration and parahydrogen and orthodeuterium conversion over palladium: Kinetics and mechanism.* Journal of Catalysis, 1966. **5**(1): p. 1-17.

6 Scholten, J.J.F. and J.A. Konvalinka, *Hydrogen-deuterium equilibration and parahydrogen and orthodeuterium conversion over palladium: Kinetics and mechanism.* Journal of Catalysis, 1966. **5**(1): p. 1-17.

7 Kay, B.D., C. Peden, H. F., and D.W. Goodman, *Kinetics of hydrogen absorption by Pd(110).* Physical Review B, 1986. **34**(2): p. 817-822.

8 Lässer, R. and G.L. Powell, *Solubility of H, D, and T in Pd at low concenctrations.* Physical Review B, 1986. **34**(2): p. 578-586.

9 Coluzzi, B., et al., *A study of diffusion of deuterium in α'-Pd deuteride by Gorsky relaxation.* Solid State Communications, 1992. **83**(8): p. 643-647.

10 Majorowski, S. and B. Baranowski, *Diffusion coefficients of hydrogen and deuterium in highly concentrated palladium hydride and deuteride phases.* Journal of Physics and Chemistry of Solids, 1982. **43**(12): p. 1119-1127.

11 Tkacz, M. and B. Baranowski, *Solubility of hydrogen in palladium hydride at high pressure of gaseous hydrogen.* Roczniki Chemii: Annales Societatis Chimicae Polonorum, 1976. **50**: p. 2159-2166.

12 Seymour, E.F.W., R.M. Cotts, and W.D. Williams, *NMR measurement of hydrogen diffusion in β-Palladium hydride.* Physical Review Letters, 1975. **35**(3): p. 165-167.

13 Powell, G.L. and J.R. Kirkpatrick, *Surface conductance and the diffusion of H and D in Pd.* Physical Review B, 1991. **43**(9): p. 6968-6976.

14 Powell, G.L., J.R. Kirkpatrick, and J.W. Conant, *Surface effects in the reaction of H and D with Pd -- Macroscopic manifestations.* Journal of the Less Common Metals, 1991. **172-174**: p. 867-872.

15 Hamilton, J., S.C. James, and W. Wolfer, *Diffusional exchange of isotopes in a metal hydride sphere*, 2011, Sandia National Laboratories: Albuquerque, NM. p. 29.

16 Wicke, E., *Isotope effects in palladium-hydrogen systems.* Platinum Metals Review, 1971. **15**(4): p. 144-146.

17 Sicking, G., *Isotope effect in metal-hydrogen systems.* Journal of the Less Common Metals, 1984. **101**: p. 169-190.

18 Sicking, G., P. Albers, and E. Magomedbekov, *Hydrogen isotope exchange and separation in gas-solid phase systems.* Journal of the Less-Common Metals, 1983. **89**(2): p. 373-391.

19 Carstens, D.H.W. and P.D. Encinias, *Hydrogen isotope exchange over palladium metal*, 1990, Los Alamos National Laboratory: Los Alamos, NM. p. 12.

20 Carstens, D.H.W. and P.D. Encinias, *Hydrogen isotope exchange in palladium hydride.* Journal of the Less-Common Metals, 1991. **172-174**(3): p. 1331-1337.

21 Powell, G.L., *Reaction probability for exchange of hydrogen isotopes on palldium.* Physical Review B, 1992. **45**(8): p. 4505-4508.

22 Trentin, V., P. Brossard, and D. Schweich, *Effects of composition on the equilibrium between hydrogen isotopes and palladium.* Chemical Engineering Science, 1993. **48**(5): p. 873-879.

23 Backman, H., et al., *Modelling of H_2/D_2 exchange over Pd.* Chemical Engineering Journal, 2005. **107**(1-3): p. 89-95.

24 Fukada, S., K. Fuchinoue, and M. Nishikawa, *Isotope separation factor and isotopic exchange rate between hydrogen and deuterium of palladium.* Journal of Nuclear Materials, 1995. **226**(3): p. 311-318.

25 Fukada, S., K. Fuchinoue, and M. Nishikawa, *Hydrogen isotope separation by displacement chromatography with palladium.* Journal of Nuclear Science and Technology, 1995. **32**(6): p. 556-564.

26 Fukada, S., H. Matsuo, and N. Mitsuishi, *Application of direct numerical analysis by Fast Fourier Transform to isotopic exchange process in a metal hydride particle bed.* Journal of Nuclear Science and Technology, 1993. **30**(2): p. 171-180.

27 Fukada, S. and M. Nishikawa, *Hydrogen isotope separation with palladium particle bed.* Fusion Engineering and Design, 1998. **39-40**: p. 995-999.

28 Foltz, G.W. and C.F. Melius, *Studies of isotopic exchange between gaseous hydrogen and palladium hydride powder.* Journal of Catalysis, 1987. **108**: p. 409-425.

29 Foltz, G.W. and C.F. Melius, *Real-time experimental measurements of isotopic exchange between gaseous hydrogen and palladium hydride powder*, 1986, Sandia National Laboratories: Albuquerque, New Mexico. p. 48.

30 COMSOL, *COMSOL Multiphysics User's Guide*, v. 4.2,http://www.comsol.com.

31 Kaviany, M., Principles of Heat Transfer in Porous Media, 2nd Edition, Springer, 1995.

32 Wilke, C.R., *A viscosity equation for gas mixtures.* Journal of Chemical Physics, 1950. **18**: p. 517.

33 Mills, A.F., *Mass Transfer*2001: Prentice-Hall. 432.

34 Larson, R.S., S.C. James, and R.H. Nilson, *Isotope Exchange Kinetics in Metal Hydrides I: TPLUG Model*, 2011, Sandia National Laboratories: Albuquerque, NM.

35 Mitacek, Jr., P. and J. G. Aston, Thw thermodynamic properties of pure Palladium and its alloys with hydrogen between 30 and 300 ^{o}K, *J. of the American Chemical Society*, 85(2), 137-141, 1963.

36 Eliassi, M., **Final memo for P&E M project, Isotope Exchange:** 164015/01.05, Modeling Foltz and Melius (1987) Isotope Exchange Experiments, Using COMSOL 4.2a, October 7, 2012.

DISTRIBUTION

Electronic Copy:

1	MS0825	Jeff Payne	1510
1	MS0899	Technical Library	9536
1	MS9035	Paul Spence	8254
1	MS9035	Brad Bon	8254
1	MS9035	Steve Rice	8254
1	MS9042	Amanda Dodd	8365
1	MS9957	Greg Wagner	8365


Sandia National Laboratories